Quarterly Journal of the Royal Meteorological Society *Q. J. R. Meteorol. Soc.* 142: 2205–2213, July 2016 A DOI:10.1002/qj.2818

RMetS
Royal Meteorological Society

Sensitivity of turbulence statistics in the lower portion of a numerically simulated stable boundary layer to parameters of the Deardorff subgrid turbulence model

Jeremy A. Gibbs[a,b]* and Evgeni Fedorovich[c]

[a]*Department of Mechanical Engineering, University of Utah, Salt Lake City, USA*
[b]*Cooperative Institute for Mesoscale Meteorological Studies, University of Oklahoma, Norman, USA*
[c]*School of Meteorology, University of Oklahoma, Norman, USA*

*Correspondence to: J. A. Gibbs, Department of Mechanical Engineering, University of Utah, 1495 E 100 S, 1550 MEK, Salt Lake City, UT 84112, USA. E-mail: jeremy.gibbs@utah.edu

Some 36 years following its creation, the Deardorff 1980 (D80) subgrid turbulence model is perhaps still the most ubiquitous scheme used in large-eddy simulation (LES) studies of atmospheric boundary-layer flows. This model is often included as the default closure scheme in a variety of codes and numerical weather prediction models. In this study, we investigate the three commonly employed corrective adjustments of the D80 closure model. These include a stability-dependent length-scale, the formulation for the subgrid turbulent Prandtl number, and the enhancement of near-surface dissipation. We implement a modified formulation of the D80 closure, then compare simulated flow statistics in the lower portion of a representative nocturnal stable boundary layer (SBL) case from LES with realistic forcing using the original D80 scheme and the modified version of the scheme. LES data were compared with observations from the Southern Great Plains (SGP) site of the Atmospheric Radiation Measurement (ARM) Program in Lamont, Oklahoma. The modified scheme shows overall improvement in reproducing vertical profiles of wind speed and potential temperature in the near-surface region of the SBL. Conclusions regarding turbulence kinetic energy and friction velocity are not as definitive, although there are signs of improved agreement with measurement data. Examination of the stability parameter and near-surface sensible heat flux suggests the modified scheme better captures effects of stability in the considered flow case. The proposed modification offers a more straightforward and interpretable framework for the parametrization of subgrid turbulence in LES of atmospheric boundary layers.

Key Words: large-eddy simulation; stable boundary layer; subgrid turbulence closure

Received 28 May 2015; Revised 24 March 2016; Accepted 7 April 2016; Published online in Wiley Online Library 25 May 2016

1. Introduction

Early atmospheric numerical modelling studies mostly focused on large-scale flows. It was desirable to treat the problems as quasi-two-dimensional and to ignore the effects of turbulence given the limited computational capacity that existed at the time. In a seminal study, Lilly (1967) eloquently explained the benefits of expanding simulations into three dimensions in order to consider additional flow types, such as turbulent flows in the atmospheric boundary layer. Lilly substantiated the need to apply numerical codes at a grid spacing small enough to accommodate the full breadth of boundary-layer turbulent scales, while acknowledging the hopelessness of the computational requirements to fully do so. Following this realization, Lilly formalized the idea of the modern large-eddy simulation (LES), that is separating simulated flow motion into resolvable- and subgrid-scale components, provided that the resolvable-scale range contains a majority of the fluid system's kinetic energy, whilst the grid spacing is placed within the inertial-subrange scale of motions (Kolmogorov, 1941), so that the subgrid turbulence may be considered isotropic (at least in an approximate sense).

Though the subgrid scales of motion are supposed to be much smaller than the resolved scales and carry much less energy, their importance was explicated by Lilly. These small-scale motions play a critical role in the transfer of kinetic energy from the resolved-scale motions to the motions within the microscale range where dissipation of kinetic energy into heat takes place. In particular, accurate reproduction of the subgrid-scale motions should ensure that the model extracts a proper amount of kinetic energy such that the modelled energy transfer adheres to the Kolmogorov energy cascade (Higgins *et al.*, 2004).

The transport equation for subgrid turbulence kinetic energy (STKE; Lilly, 1967; Piomelli and Chasnov, 1996; Wyngaard, 2010) E is given by

$$\frac{\partial E}{\partial t} = -\frac{\partial\left(\overline{u}_j E\right)}{\partial x_j} - \frac{1}{2}\tau_{ij}^{\mathrm{S}}\left(\frac{\partial \overline{u}_i}{\partial x_j} + \frac{\partial \overline{u}_j}{\partial x_i}\right) + \frac{\partial\left(\tau_{ij}^{\mathrm{S}}\overline{u}_i\right)}{\partial x_j} - \frac{1}{2}\frac{\partial}{\partial x_j}\left(\overline{u_i u_i u_j} - \overline{u}_i\overline{u}_i\overline{u}_j\right) - \frac{\partial}{\partial x_j}\left(\overline{\pi u_j} - \overline{\pi}\,\overline{u}_j\right) + \nu\frac{\partial^2 E}{\partial x_j^2} - \nu\left(\overline{\frac{\partial u_i}{\partial x_j}\frac{\partial u_i}{\partial x_j}} - \frac{\partial \overline{u}_i}{\partial x_j}\frac{\partial \overline{u}_i}{\partial x_j}\right), \tag{1}$$

where t is time, u_i ($i = 1$–3) are the velocity components along coordinate directions x_i (horizontal x_1 and x_2, and vertical x_3), $\tau_{ij}^{\mathrm{S}} = \overline{u_i u_j} - \overline{u}_i\overline{u}_j = (2/3)\delta_{ij}E + \tau_{ij}^{\mathrm{s}}$ is the subgrid kinematic momentum flux tensor (τ_{ij}^{s} is the deviatoric part of τ_{ij}^{S}), $E = 0.5\tau_{ii}^{\mathrm{S}}$, π is the normalized by density pressure deviation from the environmental (hydrostatic) value, ν is kinematic viscosity, and overbars represent filtered (resolved-scale) quantities.

Missing from Lilly's original formulation for E balance was the subgrid buoyancy production/ destruction term, which is crucial for most atmospheric boundary-layer considerations. To account for buoyancy effects, the subgrid kinematic buoyancy flux $B_i^{\mathrm{S}} = \overline{u_i b} - \overline{u}_i\overline{b}$ should be added to Eq. (1) as a source/sink term. Here, $b = \beta\theta$ is buoyancy, $\beta = (g/\theta_0)$ is the buoyancy parameter, g is gravitational acceleration, θ_0 is a constant reference value for potential temperature (the Boussinesq approximation is assumed), and θ is the potential temperature deviation from the prescribed environmental value.

Equation (1) cannot be used to close the LES problem in its original form due to the presence of third-order moments and other terms that are not solvable *a priori*. Deardorff (1980) (hereafter D80) proposed a parametrized version of Eq. (1), where production and transport terms were parametrized through the subgrid turbulent diffusivities for momentum (K_m) and heat (K_h). According to this approach, the subgrid fluxes are expressed through the gradients of resolved-scale velocity and buoyancy fields as

$$\tau_{ij}^{\mathrm{S}} = \frac{2}{3}\delta_{ij}E - K_m\left(\frac{\partial \overline{u}_i}{\partial x_j} + \frac{\partial \overline{u}_j}{\partial x_i}\right), \tag{2}$$

$$B_i^{S} = -K_h\frac{\partial \overline{b}}{\partial x_3}. \tag{3}$$

The parametrized form of Eq. (1) according to D80 is

$$\frac{\partial E}{\partial t} + \frac{\partial \overline{u}_j E}{\partial x_j} = 2K_m S_{ij}S_{ij} - K_h\frac{\partial \overline{b}}{\partial x_3} + \frac{\partial}{\partial x_j}2K_m\frac{\partial E}{\partial x_j} - \epsilon_\nu, \tag{4}$$

where

$$S_{ij} = \frac{1}{2}\left(\frac{\partial \overline{u}_i}{\partial x_j} + \frac{\partial \overline{u}_j}{\partial x_i}\right)$$

is the strain rate of the filtered velocity field, and

$$\epsilon_\nu = \nu\left(\overline{\frac{\partial u_i}{\partial x_j}\frac{\partial u_i}{\partial x_j}} - \frac{\partial \overline{u}_i}{\partial x_j}\frac{\partial \overline{u}_i}{\partial x_j}\right)$$

is the STKE dissipation rate.

Expressions are needed for K_m, K_h, and ϵ_ν in order to complete the subgrid-scale turbulence parametrization. D80 accomplished this by relating the subgrid diffusivity for momentum to the STKE and subgrid turbulence length-scale ℓ through a Prandtl–Kolmogorov-type relationship,

$$K_m = C_k\ell\sqrt{E}, \tag{5}$$

and taking K_h proportional to K_m in the form:

$$K_h = \left(1 + 2\frac{\ell}{\Delta}\right)K_m, \tag{6}$$

where C_k is a dimensionless coefficient ($= 0.1$ in D80) and $\Delta = (\Delta x_1\Delta x_2\Delta x_3)^{1/3}$ is the effective grid spacing. Although Deardorff primarily focused his LES on convective boundary layers (CBLs), the consideration of hydrostatic stability in the flow was important as he needed to represent the effects of the capping inversion overlying the CBL. As such, stratification effects were accounted for when prescribing the subgrid length-scale in the following manner:

$$\ell = \begin{cases} \Delta & \dfrac{\partial \overline{b}}{\partial x_3} \le 0, \\ \min\left[\Delta, \frac{1}{2}\dfrac{\sqrt{E}}{N}\right] & \dfrac{\partial \overline{b}}{\partial x_3} > 0, \end{cases} \tag{7}$$

where $N = \sqrt{\partial \overline{b}/\partial x_3}$ is the Brunt–Väisälä frequency.

The effective grid spacing (50 m) in the D80 numerical simulations was rather large from the current perspective. Under stable stratification, therefore, it was sensible to expect the subgrid turbulence length-scale to be smaller than the effective grid spacing. The coefficient used to define ℓ in Eq. (7) was originally set to 0.76. Here we use 0.5, a modification suggested by Nieuwstadt (1990), though the coefficient value was never formally justified (Schumann, 1991).

Finally, the STKE dissipation rate was parametrized as

$$\epsilon_\nu = C_e\frac{E^{\frac{3}{2}}}{\ell}, \tag{8}$$

where

$$C_e = f_c\left(0.19 + 0.51\frac{\ell}{\Delta}\right)$$

is a dimensionless parameter and f_c is a function designed to enhance near-wall dissipation as

$$f_c = 1 + \frac{2}{\left(\dfrac{z_{\mathrm{w}}}{\Delta z_{\mathrm{w}}} + 1.5\right)^2 - 3.3},$$

where z_{w} is the distance to the wall and Δz_{w} is the vertical size of the computational cell nearest to the wall. The description of the near-wall enhancement of dissipation in D80 leaves its implementation to interpretation. Specifically, D80 states 'Close to the surface, however, C_e was increased by a 'wall-effect' factor of up to 3.9 to prevent E from becoming unduly large there' (using our notation). Some later studies (e.g. Moeng, 1984) merely set $C_e = 3.9$ at the first model level. Our implementation shown above follows that of Nieuwstadt (1990). We feel it is more physically meaningful in the spirit of the D80 specification. Together, Eqs (2)–(8) represent a complete subgrid turbulence closure model.

Even 36 years after its development, the D80 turbulence closure is perhaps the most widely used in LES of geophysical boundary layers. Despite the advent of dynamic subgrid turbulence closures (e.g. Germano *et al.*, 1991; Lilly, 1992; Wong and Lilly, 1994; Porté-Agel, 2000, 2004; Bou-Zeid *et al.*, 2005; Basu and Porté-Agel, 2006; Kirkil *et al.*, 2012), many popular numerical codes (e.g. the Weather Research and Forecasting, WRF, model; Skamarock *et al.*, 2008) still use the Deardorff closure, although the Lilly–Smagorinsky closure (Smagorinsky, 1963; Lilly, 1967) is sometimes employed as an alternative. As a consequence, many of the assumptions and adjustments implemented in the original D80 closure formulation have been carried into the present age.

In this study, we examine three common corrective features of the D80 closure and investigate how they affect the turbulence regime in an archetypal nocturnal stable boundary layer (SBL).

First, we examine whether the closure requires the stability-dependent turbulence length-scale. One may assume that the stratification correction is unnecessary provided that the grid spacing is small enough to match, at least approximately, the reduced turbulence length-scale. Second, our own experience has shown that assuming the K_m to K_h ratio (Prandtl number, Pr) in the way it is done in D80 may cause spurious patchiness of the resolved flow fields associated with local stability changes. We suggest a new formulation for Pr, with K_h kept equal to K_m under stable conditions, and examine its impact on the simulated turbulence regime. Finally, we investigate the need of enhancement of the near-wall dissipation. Ideally, if the vertical grid spacing is sufficiently small, there should be no need to artificially increase dissipation to control TKE production near the surface. While no need to enhance dissipation is presupposed in other studies (e.g. Moeng *et al.*, 2007), we attempt to quantify the effect.

Description of the experimental set-up is given in section 2. Results are presented and discussed in section 3. Summary and conclusions follow in section 4.

2. Experimental design

2.1. Modified subgrid-scale closure

We operate under the assumption that, if a LES is carried out with a sufficiently small grid spacing, then the turbulence length-scale may be taken independent of stability. There is historical evidence to back up this assumption as provided in Schumann (1991), who found that the length-scale given by Eq. (7) exaggerated the effects of stratification manifested through an overrepresentation of dissipation and an underrepresentation of mechanical mixing. It was recommended that the length-scale be set equal to the grid spacing everywhere except for the term involving vertical diffusion of heat. We follow this guidance explicitly by setting $\ell = \Delta$ in Eqs (5) and (8), and implicitly through the adopted formulation for the Prandtl number (see below).

Based on Eqs (5) and (6), the subgrid turbulent Prandtl number in D80 is given by

$$Pr = \left(1 + 2\frac{\ell}{\Delta}\right)^{-1}. \tag{9}$$

Under the considerations of Eq. (7),

$$Pr = \begin{cases} 1/3 & \dfrac{\partial \overline{b}}{\partial x_3} \le 0, \\ \to 1 \text{ as } \ell \to 0 & \dfrac{\partial \overline{b}}{\partial x_3} > 0. \end{cases} \tag{10}$$

This means that, under stable conditions with $\ell < \Delta$, K_m is persistently smaller than K_h, while most studies (e.g. Ohya, 2001; Grachev *et al.*, 2007; Zilitinkevich *et al.*, 2012) show that, at least with moderate stability, the turbulent Pr remains approximately constant and close to one. Apart from this, our experience indicates that the original D80 formulation for K_h can lead to problematically large patchiness in the resolved flow fields where vertical buoyancy gradients in the adjoining grid cells are of opposite sign. In this case, Pr according to D80 can abruptly change when stratification switches from weakly unstable to weakly stable, or reverse. In essence, since the D80 subgrid length-scale was presupposed to be smaller than the grid spacing under stable stratification, it would be logical to parametrize the scale transition within the stable stratification regime. Conversely, since we presume in this study that $\ell = \Delta$ for any stratification, it makes more sense to handle this transition in the unstable regime while adopting for the stable regime $K_h = K_m$. In other words, we set the turbulent Prandtl number as

$$Pr = \begin{cases} \left(3 - 2\mathrm{e}^{-Ri^2}\right)^{-1} & \dfrac{\partial \overline{b}}{\partial x_3} \le 0, \\ 1 & \dfrac{\partial \overline{b}}{\partial x_3} > 0, \end{cases} \tag{11}$$

where Ri is the gradient Richardson number given by

$$Ri = \frac{\dfrac{\partial \overline{b}}{\partial x_3}}{\left(\dfrac{\partial \overline{u}_1}{\partial x_3}\right)^2 + \left(\dfrac{\partial \overline{u}_2}{\partial x_3}\right)^2}.$$

This new formulation results in a gradual decrease in K_h as the flow approaches stable stratification and K_h becoming equal to K_m at $Ri = 0$. Taking $Pr = 1$ for the stable regime is consistent with past numerical studies (e.g. Brown *et al.*, 1994) and allows us to implicitly follow the suggestion of Schumann (1991). Instead of using a stability-dependent length-scale in the expression for K_h, we define Pr in such a way that the relative effect of mechanical mixing is enhanced with stable stratification compared to the original formulation of D80.

Finally, we suggest that the near-wall enhancement of the STKE dissipation rate is unnecessary, provided that the grid spacing is adequately small. This is in line with the study by Moeng *et al.* (2007) and effectively corresponds to setting $f_c = 1$ in Eq. (8).

In summary, we solve Eq. (4) using the following modified formulations for the subgrid turbulence parameters:

$$K_m = C_k \Delta \sqrt{E}, \tag{12}$$

$$K_h = \begin{cases} \left(3 - 2\mathrm{e}^{-Ri^2}\right) K_m & \dfrac{\partial \overline{b}}{\partial x_3} \le 0, \\ K_m & \dfrac{\partial \overline{b}}{\partial x_3} > 0, \end{cases} \tag{13}$$

$$\epsilon_v = 0.7 \frac{E^{\frac{3}{2}}}{\Delta}. \tag{14}$$

2.2. LES configurations

Numerical experiments were carried out using the University of Oklahoma LES (OU-LES; Fedorovich *et al.*, 2001, 2004a) – a derivative of the Delft University LES code (Nieuwstadt, 1990) from which several other currently employed atmospheric LES codes also stem (e.g. Heus *et al.*, 2010). The OU-LES code solves the filtered Boussinesq-approximated Navier–Stokes equations of motion and thermal energy (buoyancy transport) equation. Advection/convection terms are approximated using second-order centred finite differences. Discretized equations are integrated in time using a third-order Runge–Kutta scheme implemented after Sullivan *et al.* (1996).

Simulations (Table 1 gives details) were conducted in a $(X_1 \times X_2 \times X_3) = (1.28 \times 1.28 \times 3)$ km numerical domain with a uniform grid spacing of $\Delta x_1 = \Delta x_2 = \Delta x_3 = 10$ m. This

Table 1. Simulation configurations.

Simulation	ℓ	K_m	K_h	ϵ_v
C1	$\frac{1}{2}\frac{\sqrt{E}}{N}$	$C_k \ell \sqrt{E}$	$\left(1+2\frac{\ell}{\Delta}\right)K_m$	$C_e \frac{E^{\frac{3}{2}}}{\ell}$
C2	Δ	$C_k \Delta \sqrt{E}$	K_m	$0.7\frac{E^{\frac{3}{2}}}{\Delta}$

Mesh size = 128 × 128 × 300; spacing = 10 m

particular grid spacing was chosen as a compromise between the constraint of computational expense and the need to realistically resolve small-scale turbulent flow features, since using a resolution that is too fine might inhibit proper testing of the subgrid model as most turbulence would be contained in the resolved scales. Supportive of this choice, Beare *et al.* (2006) found in a SBL LES intercomparison study that simulations using a grid spacing of 12.5 m and less were successful in sustaining resolved turbulence with a reasonable accuracy.

The simulation domain was centred over the Southern Great Plains (SGP) observational site of the Atmospheric Radiation Measurement (ARM) Program in Lamont, Oklahoma (https://www.arm.gov/sites/sgp; accessed 27 April 2016). Lateral boundary conditions for prognostic flow variables and the pressure perturbation were periodic. A sponge layer was implemented in the upper 20% of the domain to mitigate wave reflection. Monin–Obukhov similarity relationships were locally applied at the lower boundary to relate dynamic and thermal properties of the flow in the near-surface region.

A total of four simulations were conducted for the time period from 1800 UTC on 19 December 2010 to 1800 UTC on 20 December 2010. This case was selected as a representative example of the nocturnal SBL for the reasons discussed below. Two simulations each were performed with the D80 closure (henceforth denoted as C1) and using the proposed modified version of the closure (henceforth denoted as C2). Of the two simulations, one was run with the lower thermal boundary specified in terms of kinematic heat flux, and the other specified in terms of potential temperature. For purposes of this study, we will only show results from the simulations using potential temperature as the lower boundary condition. The conducted numerical tests indicate poor agreement of computed near-surface potential temperature and turbulence parameters with observational data when using the heat flux condition. In particular, potential temperature values were overpredicted, while TKE and friction velocity were underestimated. Such behaviour of the flux condition is a known issue in simulations of the SBL, as was extensively discussed in previous studies (van de Wiel *et al.*, 2007; Basu *et al.*, 2008; Gibbs *et al.*, 2015).

The timeframe for the simulations was chosen to encompass the transition from a well-developed daytime CBL into the nocturnal SBL. The D80 scheme is known to perform well in the former flow type (Fedorovich *et al.*, 2004b; Botnick and Fedorovich, 2008; Gibbs *et al.*, 2011; Gibbs and Fedorovich, 2014), while its applicability in the latter is questionable and is the subject of the current study. The first 6 h of the simulation window represent a spin-up stage designed to reach a well-established convective regime in the boundary layer before proceeding into the nocturnal SBL. Since we primarily focus on the performance of our LES for the nocturnal SBL, flow statistics have been evaluated over the time period from 0000 UTC to 1200 UTC on 20 December 2010. The observed sensible heat flux was consistently negative and variable in magnitude during this period (Figure 1).

A WRF model run with a horizontal grid spacing of 2 km was carried out for the period from 0000 UTC on 19 December to 1800 UTC on 20 December 2010 to supply each simulation with initial profiles of horizontal velocity components (u, v), potential temperature (θ), and water vapour mixing ratio (q). The evolution of the geostrophic wind was taken into account separately, through time-dependent geostrophic wind components (Eq. (15)) plugged into the resolved horizontal momentum equations. The additional 18 h period that preceded the start of the C1 and C2 simulations was allowed to properly account for spin-up adjustments in the WRF model. The normalized vertical pressure coordinate levels in the WRF model were prescribed using the hypsometric equation with observed surface pressure data and a constant vertical increment Δz (Mirocha *et al.*, 2014). Although the resulting vertical grid had only a quasi-regular vertical grid spacing of 10 m due to the approximate nature of this procedure, it served as a reasonable analogue to the OU-LES vertical grid layout.

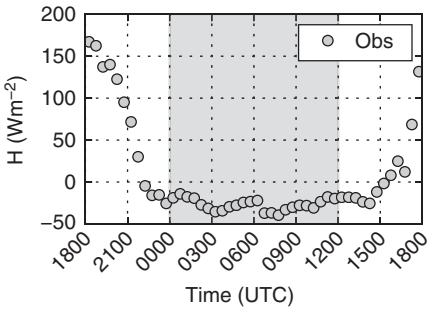

Figure 1. Sensible heat flux measured by the ECOR system (Cook, 2011) at the ARM SGP site from 1800 UTC 19 December to 1800 UTC 20 December 2010. The shaded region represents the timeframe over which comparisons were made.

These profiles of u, v, θ, and q were computed every minute by taking the spatial average over the four grid cells in the centre of the WRF model numerical domain. This averaging area roughly corresponds to the spatial extent of the OU-LES numerical grid. Following the procedure outlined in Botnick and Fedorovich (2008), these four grid cells were also used to calculate horizontal gradients of pressure, and thus to derive the geostrophic wind components as:

$$u_{\mathrm{g}} = -\frac{1}{\rho f}\frac{\partial p}{\partial y}, \qquad v_{\mathrm{g}} = \frac{1}{\rho f}\frac{\partial p}{\partial x}, \tag{15}$$

where ρ is the density of dry air, $f = 2\Omega \sin\phi$ is the Coriolis parameter, Ω is the angular velocity of Earth, $\phi = 36.6^{\circ}$ is the latitude of the ARM SGP site, and p is pressure.

As described in Gibbs *et al.* (2011), OU-LES must account for larger-scale atmospheric variability. The solutions at each time step for u, v, θ, and q were adjusted by the temporally interpolated profiles from the WRF model through a simple Newtonian nudging procedure. A nudging tendency was included in the filtered LES equation as:

$$\left(\frac{\partial \widetilde{\psi}}{\partial t}\right)_{\mathrm{n}} = -\frac{\overline{\widetilde{\psi}}_{\mathrm{LES}} - \psi_{\mathrm{WRF}}}{\alpha_{\mathrm{n}}}, \tag{16}$$

where $\widetilde{\psi}$ is the considered resolved flow variable, $\left(\partial \widetilde{\psi}/\partial t\right)_{\mathrm{n}}$ is its tendency due to nudging, $\overline{\widetilde{\psi}}_{\mathrm{LES}}$ is the horizontal mean vertical profile of $\widetilde{\psi}$ taken from the preceding time step, ψ_{WRF} is the corresponding profile from the WRF model at that time step, and $\alpha_{\mathrm{n}} = 3600$ s is the nudging time constant. Thus, the tendencies of u, v, θ, and q are adjusted across the entire domain at every time step. This is accomplished by subtracting the difference between the domain-averaged profiles from OU-LES and the local profiles from the WRF model. The difference is further scaled by a time constant, which controls the rate of adjustment of the spatially averaged OU-LES fields to the WRF model profiles that carry information on the larger-scale atmospheric variability. Finally, the thermal boundary condition at the surface was prescribed using the time series of 2 m potential temperature, also taken from the WRF model output.

While it appears more sensible to initialize the model and prescribe the lower boundary condition using observational data from the ARM site, this procedure proved problematic for two reasons. First, there are no ARM data that can be used to reliably describe the vertical profiles of atmospheric quantities over the entire depth of the numerical domain. This necessitates the use of vertical profiles from the WRF model. Second, there are often notable mismatches between the observed surface values of potential temperature and the corresponding near-surface values retrieved from the WRF model. These mismatches produce local regions of erroneous near-surface instability during the night hours. Such spurious behaviour apparently results from the combined effects of comparing grid volumes with point

measurements and from internal bias due to the inadequate performance of the WRF model under stable conditions. As discussed later in section 3.2, we attempt to mitigate these undesirable effects through the use of alternative comparison techniques.

2.3. Observational data

Simulated values of mean meteorological variables, such as potential temperature and wind speed, were compared with observational data from the ARM Surface Meteorology Systems (MET) station (Ritsche and Prell, 2011). The MET system measures temperature at 2 m above ground level (agl) and wind speed at 10 m agl. The corresponding values from OU-LES were extrapolated from the first model level, located at 5 m agl, to the respective observation height using Monin–Obukhov similarity relationships (Monin and Obukhov, 1954).

Simulated turbulence statistics, such as TKE and turbulent stress (represented by friction velocity u_*), were compared with observations taken by the ARM Eddy Correlation Flux Measurement System (ECOR; Cook, 2011) and Carbon Dioxide Flux Measurement System (CO2FLX; Fischer, 2005). The ECOR system measures turbulent fluxes at 3 m agl, while the CO2FLX system takes similar measurements at 4, 25, and 60 m agl. These turbulence data were directly compared with the corresponding OU-LES statistics, which were computed at 5 m agl.

3. Results

3.1. Internal differences

In order to understand and quantify the performance of the modified subgrid closure presented by Eqs (12)–(14), we compare results from the simulations employing the original (C1) and modified (C2) versions of the D80 closure. First we look at these differences as explicated by the near-surface (within the lowest 100 m agl) vertical profiles of the mean-flow parameters and turbulence statistics. These profiles represent the values of the respective quantities computed by temporal averaging over the period from 0000 to 1200 UTC on 20 December 2010.

Profiles of mean horizontal wind speed and potential temperature are shown in Figure 2(a, b) respectively. For horizontal wind speed, there is little difference between simulations, though there is a visual hint that the vertical gradient of wind speed in the lowest portion of the SBL is reduced in the C2 case. However, noticeable differences exist for potential temperature, where the C2 profile points to the increased near-surface gradient and the reduced near-surface value of potential temperature. The increased vertical mixing of momentum and stronger stratification in the lower portion of the SBL simulated with the modified closure is expected because K_m is larger in the C2 case as a result of setting $\ell = \Delta$, while the relative influence of K_h is reduced through the new formulation of Pr given by Eq. (11).

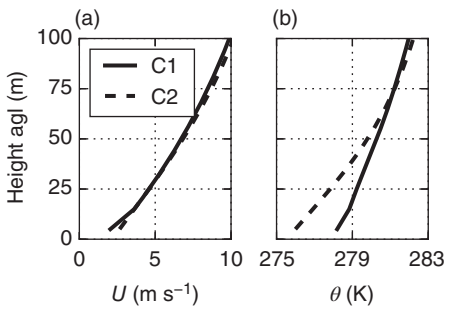

Figure 2. Near-surface vertical profiles of (a) wind speed and (b) potential temperature. Profiles represent mean quantities over the time period from 0000 to 1200 UTC on 20 December 2010.

Differences in TKE between the C1 and C2 simulations may be assessed from data shown in Figure 3(a)–(c). There is a distinct reduction in resolved turbulence kinetic energy (RTKE; (a)) throughout the lowest 100 m in the C2 simulation. Conversely, the STKE (b) is largest for the C2 case throughout the near-surface region, with the maximum increase very close to the surface, although the overall differences between results from the two simulations are minimal. Finally, the total turbulence kinetic energy (TKE; (c)) remains almost unchanged near the surface, while the TKE values from the C1 simulation are markedly larger throughout the lowest 100 m.

The observed changes in RTKE may be explained, at least in part, by considering the C1 and C2 formulations for K_m. It follows from Eqs (5) and (12) that K_m is clearly larger for the C2 configuration. The resulting enhanced subgrid mixing leads to reduced spatial variability in the resolved velocity fields and thus smaller values of the RTKE.

The increase in near-surface STKE may be understood by examining how changes in the subgrid formulations for K_m and K_h can affect the STKE balance, Eq. (4). To illustrate this, we apply the C1 and C2 formulations in the STKE balance equation for an instantaneous flow state represented by constant values of STKE, E_0, and shear, $(S_{ij}S_{ij})_0$, assume that the flow is sufficiently stratified such that $\ell = \sqrt{E_0}/2N$, and consider the differences between the STKE tendency terms:

$$\left(\frac{\partial E}{\partial t}\right)_{C2} - \left(\frac{\partial E}{\partial t}\right)_{C1} = D(\Delta - \ell) - F\left(\frac{\Delta^2}{\ell^2} - \frac{\Delta}{\ell} - 2\right) - G\left\{0.7 - f_c\left(0.19\frac{\Delta}{\ell} + 0.51\right)\right\}, \quad (17)$$

where $D = 2C_k(S_{ij}S_{ij})_0\sqrt{E_0}$, $F = C_k\sqrt{E_0^3}/4\Delta$, and $G = \sqrt{E_0^3}/\Delta$. Equation (17) demonstrates how the time tendencies of STKE differ between the two configurations. The three terms on the right-hand side represent the differences attributed to shear, buoyancy, and dissipation, respectively. In the case where $\ell = \Delta$, the difference reduces to $2F - G(0.7 - 0.7f_c)$. Since f_c is maximized at the first model level and tends to unity far away from the surface, the expression may be rewritten as $2F + I > 0$. This means that STKE would be larger in the C2 configuration. As stability increases in C1 ($\ell < \Delta$), the shear and dissipation terms will always lead to the increase of STKE. However, the contribution from the buoyancy term is dependent on the ratio of Δ to ℓ. The buoyancy term results in no change to STKE when $\Delta/\ell = 2$, and acts as a source when $\Delta/\ell < 2$. Oppositely, the term acts as a sink when $\Delta/\ell > 2$, which is almost always the case under the considered stability conditions. Because $K_h(\mathrm{C2}) > K_h(\mathrm{C1})$ according to the new Pr formulation, Eqs (11) and (13), stratification in the C2 case acts to reduce the STKE production more than in the C1 case. Even so, the enhanced subgrid mechanical mixing associated with increased K_m, coupled with decreased dissipation, leads to a net increase in STKE in the C2 case as compared to C1.

Another notable feature present in the mean profile of TKE for the C1 case is the kink located at 15 m agl. This peak apparently results from the enhanced near-wall dissipation in the D80 closure, which produces maximum dissipation enhancement at the first model level. Since dissipation correction drops with height relatively fast, there is a sharp increase in STKE already at the second model level. With no dissipation correction in the C2 simulation, the kink disappears, and the TKE reaches maximum values at the level closest to the surface.

3.2. Comparison with observations

In order to ascertain whether the differences between the results of the C1 and C2 simulations discussed in the previous section are physically meaningful, we compare the data from these simulations with observations from the ARM SGP site.

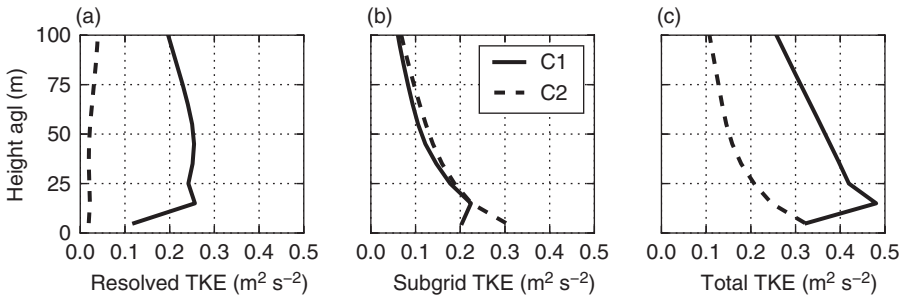

Figure 3. Near-surface vertical profiles of (a) resolved TKE, (b) subgrid TKE, and (c) total TKE. Profiles represent mean quantities over the time period from 0000 to 1200 UTC on 20 December 2010.

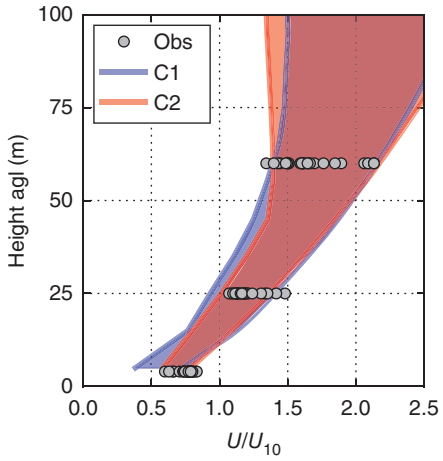

Figure 4. Normalized horizontal wind speed at 4, 25, and 60 m agl from the ARM SGP CO2FLX system and OU-LES data over the time period from 0000 to 1200 UTC on 20 December 2010. Grey circles represent measurement data. Blue and red areas represent the data ranges of the C1 and C2 simulations, respectively, while the magenta area represents their overlap.

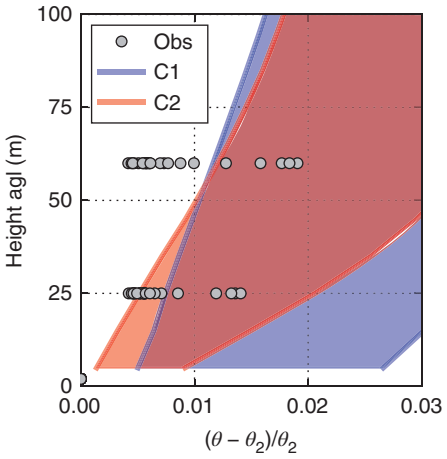

Figure 5. Normalized potential temperature at 2, 25, and 60 m agl from the ARM SGP MET system and OU-LES data over the time period from 0000 to 1200 UTC on 20 December 2010. Other details are as Figure 4.

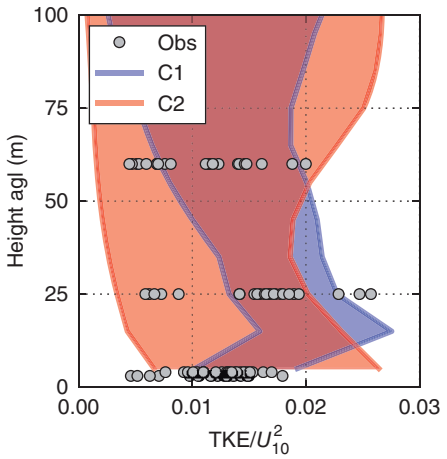

Figure 6. Normalized total TKE at 3 m agl from the ARM SGP ECOR system, and at 4, 25, and 60 m agl from the ARM SGP CO2FLX system, and OU-LES data over the time period from 0000 to 1200 UTC on 20 December 2010. Other details are as Figure 4.

Comparisons of this type are notoriously problematic because the value from a model grid cell represents an implied spatial average over the cell, while an observation is a localized measurement often obtained by averaging in time. Another issue in this case is model bias, either inherent to OU-LES, or externally imposed through the nudging to the WRF model profiles. In order to highlight the effects of the statistical uncertainty, we compare flow parameters from OU-LES to their observed counterparts by showing the variability ranges throughout the entire nocturnal SBL stage (section 2.2). We present the compared flow parameters being normalized by relevant scales to mitigate the influence of model bias.

The simulated and observed wind-speed profiles are presented in Figure 4. Observations from the CO2FLX system are shown at 4, 25, and 60 m agl for the considered time period (0000–1200 UTC on 20 December 2010). Data ranges for the C1 and C2 simulations over this timeframe are depicted as blue and red areas, respectively, and the overlapping areas are given in magenta. The areas overlap at most levels, but the data spread is reduced for the C2 simulation. This reduced variability of wind speed better matches observational data, especially near the surface. Such a feature is consistent with the previously discussed increase in near-surface wind speed caused by enhanced mixing in the C2 simulation (Figure 2).

The corresponding potential temperature distributions are shown in Figure 5. Observations from the MET tower are presented at 4, 25, and 60 m agl for the entire period of interest. Results for the temperature are less consistent than for the wind speed. The C2 simulation results in the reduced variability of potential temperature values compared to the C1 simulation. The C2 simulation also produce smaller values of temperature at the lower levels, in better agreement with observations. This feature is consistent with a better representation of the low-level temperature gradient by the C2 simulation (Figure 2). However, at 60 m agl, over half of the observations lie outside of either the C1 or C2 data ranges. This indicates that both simulations fail to properly reproduce the vertical gradient of potential temperature above 25 m agl, supposedly due to inadequate representation of the vertical diffusion of heat controlled through K_h.

Finally, comparisons for TKE are shown in Figure 6. There is once again considerable overlap between predictions by both simulations but, unlike the cases of wind speed and potential temperature, the C2 simulation data covers a broader range of values than the C1 data. However, for a vast majority of the TKE values, both schemes perform admirably. In the areas where the predictions by the schemes diverge from each other, the C1 configuration data skew toward larger values than the C2

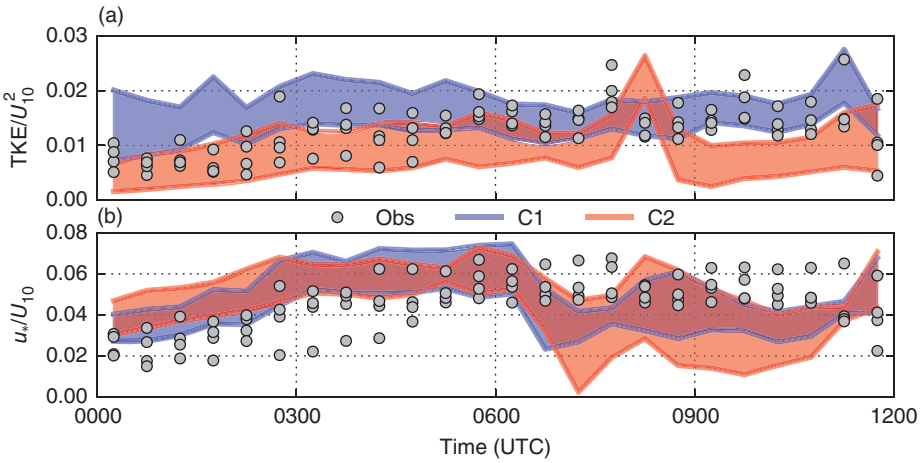

Figure 7. (a) Normalized total TKE and (b) normalized friction velocity at 3 m agl from the ARM SGP ECOR system, at 4, 25, and 60 m agl from the ARM SGP CO2FLX system, and OU-LES data over the time period from 0000 to 1200 UTC on 20 December 2010. Grey circles represent measurement data. Blue and red areas represent the data ranges in the lowest 60 m of the C1 and C2 simulations, respectively, while the magenta area represents their overlap.

data. Generally speaking, the C1 simulation data better match observations that lie outside of the overlap on the high end (for which there are few data points), while the C2 simulation data better match observations that lie outside of the overlap on the low end (for which there are far more data points).

In order to better understand the behaviour by each scheme in reproducing turbulence near the surface under stable conditions, we consider the time evolution of the TKE and friction velocity. Figure 7 shows observations from the ECOR system at 3 m agl, from the CO2FLX system at 4, 25, and 60 m agl, and OU-LES data from the C1 and C2 simulations. The coloured areas in this figure correspond to the data ranges in the lowest 60 m of each respective simulation.

There is little overlap between C1 and C2 simulation data for TKE within the first 6 h of the comparison window. During this time, the C2 simulation better captures the observed range in TKE as reported by the ARM measurement systems. There is more overlap between C1 and C2 data during the following 3 h, though the time trends of TKE predicted by each scheme substantially vary. The C1 configuration better matches the observations, though it is arguable that the C2 configuration better reflects the TKE variability if we make allowances for temporal lags between different data sources. During the final 3 h, there is very little overlap between the C1 and C2 simulation data, with the C1 configuration unequivocally yielding the better match with observations.

While the C2 simulation reproduced more realistic TKE values during the first 6 h, the same is not true for friction velocity over the same period of time. The data from the two schemes overlap over a broad range within the middle of the timeframe, although the C2 configuration generally points to a narrower range of values. Both the C1 and C2 configurations overestimate friction velocity compared to observations throughout the first 6 h. During the final 6 h of the timeframe, the data range from the C2 simulation expands dramatically, and neither simulation has a clear advantage. Data from both simulations generally underestimate friction velocity during this time window as compared to the observations. When matches do occur, they are almost always within the region of the C1 and C2 overlapped data.

To better understand whether the modifications of the C2 formulation represent an overall improvement in representing the SBL over that of the original D80 scheme, we present in Figure 8 the comparisons between observational and simulation data for two measures of stability. The stability parameter z/L is shown in Figure 8(a), where z is taken to be the height of the first model level (5 m) and the Obukhov length L is expressed as

$$L = -\frac{u_*^3}{\kappa \overline{w'B'}}, \tag{18}$$

where $\kappa = 0.4$ is the von Kármán constant and $\overline{w'B'} = \beta \overline{w'\theta'} + 0.61 g \overline{w'q'}$ is the kinematic buoyancy flux, with $\overline{w'\theta'}$ and $\overline{w'q'}$ representing the kinematic flux of heat and moisture, respectively. The heat flux H, shown in Figure 8(b), was evaluated as $\rho c_p \overline{w'\theta'}$, where c_p is the specific heat of air at constant pressure. Examination of the stability parameter shows that the C2 configuration yields a much better match with observations than does the C1 simulation, which is overpredicted throughout the entire duration of SBL. The overestimation of z/L by the C1 simulation points to an underprediction of L, which can result from a u_* that is too small or a kinematic flux of buoyancy that is too large. Recalling that the differences in u_* shown between the two configurations in Figure 7 are generally small, the most likely explanation for the improvement in z/L is the improvement in the kinematic flux of heat and moisture. Using dimensional analysis, one can show that the contribution to the buoyancy flux from heat is an order of magnitude larger than that from moisture. Thus, the improvement shown in Figure 8(a) is primarily caused by better treatment of the kinematic heat flux. This is confirmed by looking at the near-surface sensible heat flux in Figure 8(b), where the C2 simulation shows a better overall agreement with observations than does the C1 simulation.

4. Summary and conclusions

In this study, we revisit perhaps the most popular subgrid closure scheme in use for LES of atmospheric boundary-layer flows. Despite the advent of dynamic subgrid closures and the suggestion of various improvements of the D80 scheme over the past 36 years, the original Deardorff (1980) scheme is used as the default closure in a variety of popular numerical modelling tools, such as the WRF model. We examined, in the LES of a representative nocturnal SBL, the effects of three corrective parameters commonly applied in the D80 closure. These included the stability correction for the subgrid length-scale, the formulation of the ratio between subgrid diffusivity for momentum and heat (subgrid Prandtl number), and the enhancement of the near-wall dissipation. By selecting a grid spacing of 10 m, we attempted to balance the need for accuracy while ensuring that the effects of the closure still remain relevant.

Resulting differences between mean wind speed and potential temperature profiles indicate that the modified (as compared to the original D80 scheme) formulation C2 (corresponding to Eqs (12)–(14)) produces a slight increase in near-surface wind speed, indicative of enhanced mechanical mixing of momentum. This difference was found meaningful through comparisons with observations. The spread of wind speed data from the C2 simulation was reduced across the near-surface region of the SBL compared to the spread of data from the C1 simulation

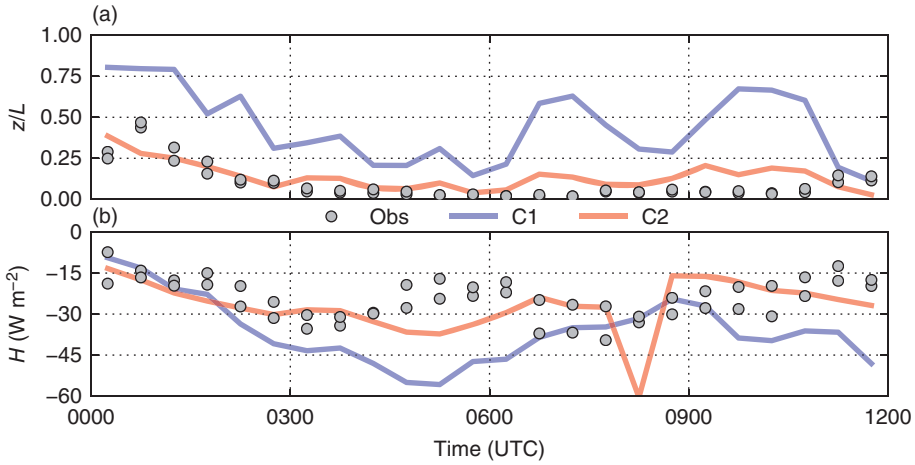

Figure 8. (a) Stability parameter z/L and (b) sensible heat flux at 3 m agl from the ARM SGP ECOR system, at 4 m agl from the ARM SGP CO2FLX system, and OU-LES data over the time period from 0000 to 1200 UTC on 20 December 2010. Grey circles represent measurement data. Blue and red lines represent data from the C1 and C2 simulations, respectively.

with the original D80 closure formulation. Such improvement was most notable at the first model level above the surface. Differences in mean potential temperature profiles point to enhanced cooling and a slightly sharper near-surface gradient of potential temperature in the C2 case, which is supported by comparisons with measurement data.

The differences in TKE between the C1 to C2 simulations are manifested by a pronounced reduction in RTKE accompanied by a notable increase in STKE very close to the surface in the C2 case. This results in an overall reduction of TKE throughout the lower region of the SBL, except for the lowest level at the surface where TKE values remained unchanged. Comparisons with observational data from the ARM SGP site offer hints of improvement of the TKE predictions by the C2 simulation, although the overall outcome is rather uncertain. The C2 simulation data seemingly better match observations on the lower end of TKE values, but the agreement is worse on the higher end of the TKE values. These findings are confirmed by the examination of the time series of observational and simulation TKE data. For friction velocity, little difference is found between C1 and C2 predictions. Both simulations overestimate friction velocity in the first half of the comparison window and underestimate it in the second half.

One might be rightfully concerned that the RTKE reduces so dramatically in the C2 simulation despite the presence of rather strong mechanical forcing. In fact, the ratio of STKE to RTKE is approximately five times larger in the C2 case than in the C1 case. These relatively small RTKE values are a consequence of the weakened local gradients of velocity that are caused by enhanced mixing in the lower portion of the SBL simulated using the modified subgrid scheme. To this end, it is unclear, however, whether the parameter adjustments incorporated in the original D80 scheme were based on some clear physical reasoning or were intended to merely produce more plausible effects close to the surface. The considerations contained within Deardorff (1980) hint that the latter is true. It is also possible that the long time averaging affects the structure of the RTKE vertical distribution. Since there are no data available on the partitioning between resolved and subgrid components of TKE in the simulated SBL case, it is impossible to make definitive conclusions in this regard.

Despite the noted difficulties in interpreting results, there is some evidence that the C2 model offers an improved representation of TKE for the employed numerical grid. Recall that the magnitude of STKE remains largely unchanged between the two configurations, except at the lowest two model levels. This feature is expected since artificial enhancement of dissipation near the surface was removed in the C2 simulation. Such behaviour suggests that the modified scheme differently distributes kinetic energy between the subgrid and resolved motions near the ground compared to the original scheme. Measurement data, on the other hand, indicate that the C2 scheme better captures TKE in the lowest 60 m of the SBL (Figure 7) over a significant portion of the simulation window. Since the STKE values do not change much between the C1 and C2 configurations, this suggests that the modified scheme more realistically represents RTKE within this time period.

While some conclusions regarding the TKE differences between the C1 and C2 cases are not definitive, there are signs of improvement of TKE predictions in the C2 simulation. However, the performance of the C2 scheme with respect to TKE degrades after 6 h, when a sharp decrease in the sensible heat flux is observed (Figure 1). Coupled with the inability of the C2 scheme to properly reproduce the potential temperature gradient at the surface, especially above 25 m agl, this points to a possible deficiency of the K_h formulation. Although the proposed changes lead to higher values of both K_m and K_h, perhaps the increase in K_h is insufficient. It would be advisable, in this connection, to further explore the parametrization of the length-scale in association with the subgrid diffusivity for heat.

Although these particular parameters do not always individually offer categorical conclusions about the relative performance of each scheme, the consideration of their combined effects through z/L is more definitive. The data shown in Figure 8 suggests that the C2 scheme better typifies effects of stability in a representative SBL through an improvement in representing the relative mechanical and buoyancy contributions. This improvement was primarily associated with better representation of the near-surface sensible heat flux when using the modified turbulence closure scheme. In our opinion, the proposed modification of the D80 scheme is appealingly straightforward and offers an interpretable framework for parametrization of subgrid turbulence in LES of atmospheric boundary-layer flows.

Acknowledgements

This material is based upon work supported by the National Science Foundation under grant no. AGS-1359698. The authors wish to thank Dr. Alan Shapiro for several discussions that improved the scope and content of this work. The authors have no conflicts of interest for this material.

References

Basu S, Porté-Agel F. 2006. Large-eddy simulation of stably stratified atmospheric boundary layer turbulence: A scale-dependent dynamic modeling approach. *J. Atmos. Sci.* **63**: 2074–2091.

Basu S, Moene AF, Holtslag AAM, Steeneveld GJ, van de Wiel BJH. 2008. An inconvenient 'truth' about using sensible heat flux as a surface boundary condition in models under stably stratified regimes. *Acta Geophys.* **56**: 88–99.

Beare RJ, MacVean MK, Holtslag AAM, Golaz JC, Jimenez MA, Khairoutdinov M, Kosović B, Lewellen D, Lund TS, Lundquist JK, McCabe A, Moene AF, Noh Y, Raasch S, Cuxart J, Esau I. 2006. An intercomparison of large-eddy simulations of the stable boundary layer. *Boundary-Layer Meteorol.* **118**: 247–272.

Botnick AM, Fedorovich E. 2008. Large-eddy simulation of atmospheric convective boundary layer with realistic environmental forcings. In *Quality and Reliability of Large-Eddy Simulations*, Meyers J, Geurts B, Sagaut P. (eds.): 193–204. Springer: Dordrecht, Netherlands.

Bou-Zeid E, Meneveau C, Parlange M. 2005. A scale-dependent Lagrangian dynamic model for large-eddy simulation of complex turbulent flows. *Phys. Fluids* **17**: 0251051, doi: 10.1063/1.1839152.

Brown AR, Derbyshire SH, Mason PJ. 1994. Large-eddy simulation of stable atmospheric boundary layers with a revised stochastic subgrid model. *Q. J. R. Meteorol. Soc.* **120**: 1485–1512.

Cook DR. 2011. 'Eddy correlation flux measurement systems handbook', Technical report DOE/SC-ARM/TR-052. US Department of Energy: Argonne, IL.

Deardorff JW. 1980. Stratocumulus-capped mixed layers derived from a three-dimensional model. *Boundary-Layer Meteorol.* **18**: 495–527.

Fedorovich E, Nieuwstadt FTM, Kaiser R. 2001. Numerical and laboratory study of horizontally evolving convective boundary layer. Part I: Transition regimes and development of the mixed layer. *J. Atmos. Sci.* **58**: 70–86.

Fedorovich E, Conzemius R, Mironov D. 2004a. Convective entrainment into a shear-free linearly stratified atmosphere: Bulk models reevaluated through large eddy simulations. *J. Atmos. Sci.* **61**: 281–295.

Fedorovich E, Conzemius R, Esau I, Chow FK, Lewellen D, Moeng C-H, Pino D, Sullivan P, de Arellano JVG. 2004b. Entrainment into sheared convective boundary layers as predicted by different large eddy simulation codes. In *Preprints, 16th Symposium on Boundary Layers and Turbulence*, Portland, ME. American Meteorological Society: Boston. P4.7, pp. 1–14.

Fischer ML. 2005. 'Carbon dioxide flux measurement systems handbook', Technical report ARM TR-048. US Department of Energy: Berkeley, CA.

Germano M, Piomelli U, Moin P, Cabot WH. 1991. A dynamic subgrid-scale eddy viscosity model. *Phys. Fluids A:* **3**: 1760. doi: 10.1063/1.857955.

Gibbs JA, Fedorovich E. 2014. Comparison of convective boundary-layer velocity spectra retrieved from large-eddy simulation and Weather Research and Forecasting model data. *J. Appl. Meteorol. Climatol.* **53**: 377–394.

Gibbs JA, Fedorovich E, van Eijk AMJ. 2011. Evaluating Weather Research and Forecasting (WRF) model predictions of turbulent flow parameters in a dry convective boundary layer. *J. Appl. Meteorol. Climatol.* **50**: 2429–2444.

Gibbs JA, Fedorovich E, Shapiro A. 2015. Revisiting surface heat-flux and temperature boundary conditions in models of stably stratified boundary-layer flows. *Boundary-Layer Meteorol.* **154**: 171–187.

Grachev AA, Andreas EL, Fairall CW, Guest PS, Persson POG. 2007. On the turbulent Prandtl number in the stable atmospheric boundary layer. *Boundary-Layer Meteorol.* **125**: 329–341.

Heus T, van Heerwaarden CC, Jonker HJJ, Siebesma AP, Axelsen S, van den Dries K, Geoffroy O, Moene AF, Pino D, de Roode SR, Vilà-Guerau de Arellano J. 2010. Formulation of the Dutch Atmospheric Large-Eddy Simulation (DALES) and overview of its applications. *Geosci. Model Dev.* **3**: 415–444.

Higgins C, Parlange MB, Meneveau C. 2004. Energy dissipation in large-eddy simulation: Dependence on flow structure and effects of eigenvector alignments. In *Atmospheric Turbulence and Mesoscale Meteorology*, Fedorovich E, Rotunno R, Stevens B. (eds.): 51–69. Cambridge University Press: Cambridge, UK.

Kirkil G, Bou-Zeid E, Chow FK, Kosović B, Mirocha J. 2012. Implementation and evaluation of dynamic subfilter-scale stress models for large-eddy simulation using WRF. *Mon. Weather Rev.* **140**: 266–284.

Kolmogorov A. 1941. The local structure of turbulence in incompressible viscous fluid for very large Reynolds' numbers. *Dokl. Akad. Nauk SSSR* **30**: 301–305.

Lilly DK. 1967. 'The representation of small-scale turbulence in numerical simulations'. In *Proceedings of the IBM Scientific Computing Symposium on Environmental Sciences, IBM form no. 320–1951. Yorktown Heights, NY, pp. 195–209.*

Lilly DK. 1992. A proposed modification of the Germano subgrid-scale closure method. *Phys. Fluids A* **4**: 633, doi: 10.1063/1.858280.

Mirocha J, Kosović B, Kirkil G. 2014. Resolved turbulence characteristics in large-eddy simulations nested within mesoscale simulations using the weather Research and Forecasting Model. *Mon. Weather Rev.* **142**: 806–831.

Moeng C-H. 1984. A large-eddy simulation for the study of planetary boundary layer turbulence. *J. Atmos. Sci.* **41**: 2052–2062.

Moeng C-H, Dudhia J, Klemp J, Sullivan P. 2007. Examining two-way grid nesting for large eddy simulation of the PBL using the WRF model. *Mon. Weather Rev.* **135**: 2295–2311.

Monin AS, Obukhov AM. 1954. Basic laws of turbulent mixing in the surface layer of the atmosphere. *Contrib. Geophys. Inst. Acad. Sci. USSR* **151**: 163–187.

Nieuwstadt FTM. 1990. Direct and large-eddy simulation of free convection. In *Proceedings of the Ninth International Heat Transfer Conference*, Jerusalem, Israel: 37–47. Hemisphere Publishing Corporation: New York, NY.

Ohya Y. 2001. Wind-tunnel study of atmospheric stable boundary layers over a rough surface. *Boundary-Layer Meteorol.* **98**: 57–82.

Piomelli U, Chasnov JR. 1996. Large-eddy simulations: Theory and applications. In *Turbulence and Transition Modelling*, Hallbäck M, Henningson DS, Johansson AV, Alfredsson PH. (eds.): 269–336. Springer: Dordrecht, Netherlands.

Porté-Agel F. 2000. A scale-dependent dynamic model for large-eddy simulation: Application to a neutral atmospheric boundary layer. *J. Fluid Mech.* **415**: 261–284.

Porté-Agel F. 2004. A scale-dependent dynamic model for scalar transport in large-eddy simulations of the atmospheric boundary layer. *Boundary-Layer Meteorol.* **112**: 81–105.

Ritsche MT, Prell J. 2011. 'Surface meteorology systems handbook', Technical report DOE/SC-ARM/TR-086. US Department of Energy: Argonne, IL.

Schumann U. 1991. Subgrid length-scales for large-eddy simulation of stratified turbulence. *Theor. Comp. Fluid Dyn.* **2**: 279–290.

Skamarock WC, Klemp JB, Dudhia J, Gill DO, Barker DM, Wang W, Powers JG. 2008 'A description of the advanced research WRF version 3', Technical report TN-475+STR. NCAR: Boulder, CO.

Smagorinsky J. 1963. General circulations experiments with the primitive equations. *Mon. Weather Rev.* **91**: 99–164.

Sullivan PP, McWilliams JC, Moeng C-H. 1996. A grid nesting method for large-eddy simulation of planetary boundary-layer flows. *Boundary-Layer Meteorol.* **80**: 167–202.

van de Wiel BJH, Moene AF, Steeneveld GJ, Hartogensis OK, Holtslag AAM. 2007. Predicting the collapse of turbulence in stably stratified boundary layers. *Flow Turbul. Combust.* **79**: 251–274.

Wong VC, Lilly DK. 1994. A comparison of two dynamic subgrid closure methods for turbulent thermal convection. *Phys. Fluids* **6**: 1016, doi: 10.1063/1.868335.

Wyngaard J. 2010. *Turbulence in the Atmosphere*. Cambridge University Press: Cambridge, UK.

Zilitinkevich SS, Elperin T, Kleeorin N, Rogachevskii I, Esau I. 2012. A hierarchy of energy- and flux-budget (EFB) turbulence closure models for stably-stratified geophysical flows. *Boundary-Layer Meteorol.* **146**: 341–373.

